

Chapter

6 | Analysis of the correlated production of strange hadrons

Following the mass measurement of multi-strange baryons in Chap. 5, the present work is complemented by a second analysis. Similarly to the first one, the latter pushes the limits of the LHC Run-2. It proposes to correlate the production of hyperons – and most particularly, Ω – and other particles produced in the event.

I Introduction

The Quark Gluon Plasma (QGP) is studied experimentally for more than two decades now, from the first hints of its existence at the SPS in the years 2000's to its fine characterisation at LHC nowadays (Sec. 2|II). It is explored through the study of its signatures and, for a long time, was considered as a well understood medium. Recently, it has been observed that small systems exhibit most of the signs usually attributed to the QGP: long range correlation in the lowest multiplicity pp collisions[167], collective flow [168][169], heavy quarkonia suppression [170]¹. This observation questions the very foundations of the QGP concept: either the QGP physics picture in heavy ion collisions must be re-designed and further rooted on pp collisions, or conversely, the QCD physics in small systems should be extended with new features to introduce collectivity. One way or the other, a better description of

¹Only the thermal photons and jet quenching signatures have not been observed in small systems (yet), whereas they are present in heavy-ion collisions. The investigation of these two signatures in small systems will be further examined in the LHC Run-3 and Run-4 [171].

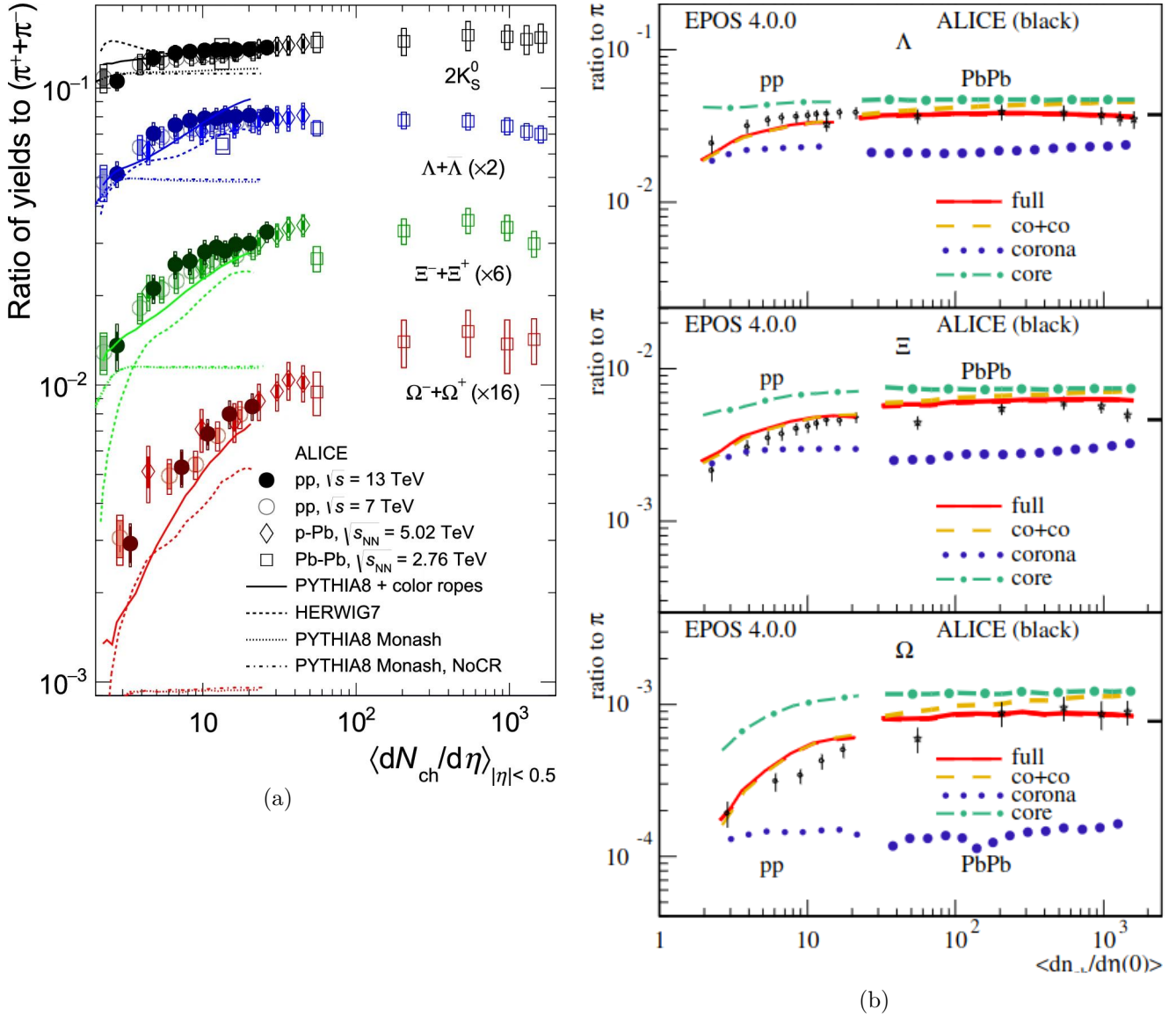


Fig. 6.1: Integrated strange hadrons-to-pions yield ratio as a function of the average charged particle multiplicity at mid-rapidity in ALICE, compared to different MC predictions. On the left, it is measured in pp at $\sqrt{s} = 7$ and 13 TeV, p-Pb at $\sqrt{s_{NN}} = 5.02$ TeV, Pb-Pb collisions at $\sqrt{s_{NN}} = 2.76$ TeV, and compared to PYTHIA 8 and HERWIG [172]; on the right, these are measurements in pp at $\sqrt{s} = 7$ TeV and Pb-Pb collisions at $\sqrt{s_{NN}} = 2.76$ TeV, with different predictions from EPOS [173].

the pp and heavy-ion collision dynamics appears as an absolute must, in order to a continuum of physics.

One of the key historical signatures of QGP is the strangeness enhancement which consists in the enhanced yield of multi-strange hadrons in heavy ion collisions with respect to small systems (Sec. 2|II-B). Such yields also scale smoothly with the charged particle multiplicity in pp collisions (Sec. 2|II-C, Fig. 2.15). Different models using fundamentally different mechanisms manage to reproduce qualitatively this trend (Fig. 6.1). On one hand, PYTHIA models the quark hadronisation using the Lund Strings; these correspond to gluon fields, that break whenever the string ten-

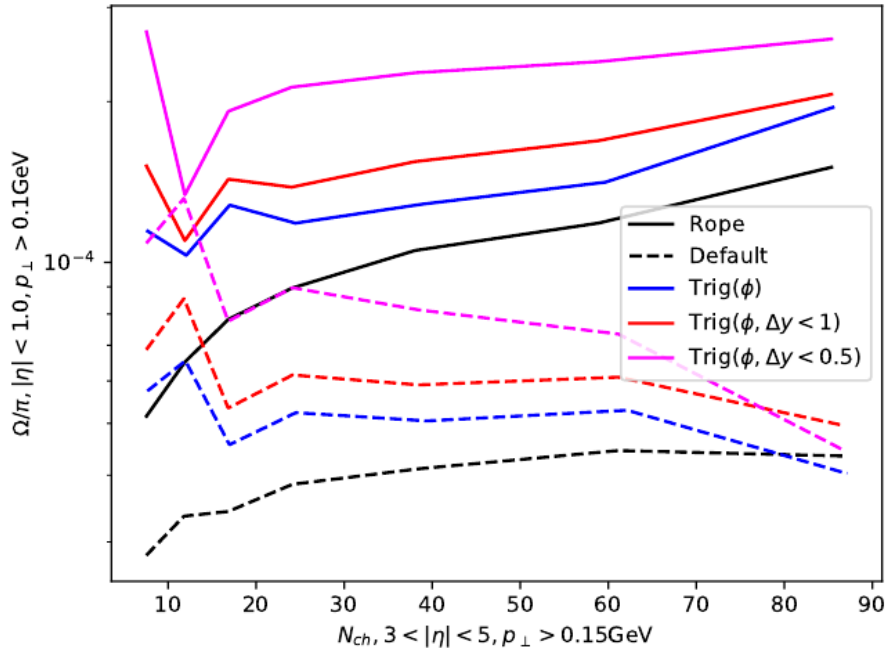


Fig. 6.2: PYTHIA 8 predictions for the Ω -to- π^\pm yield ratio as a function of the charged particle multiplicity in pp collisions at $\sqrt{s} = 13$ TeV, in presence of a $\phi(1020)$ resonance (colour lines) or not (black line). The default PYTHIA configuration (PYTHIA 8, tune: Monash 2013) is indicated in dashed line, whereas the full curves represent the case with the colour ropes enabled.

sion energy is high enough and thus leading to the formation of hadrons, similarly as in Fig. 2.7. Both pp and heavy-ion collision physics originate from the interaction of these strings, *i.e.* this approach assumes the absence of a QGP. On the other hand, EPOS relies on a core-corona model: a dense core hosting a QGP-like collective medium, surrounded by a hadron gas corona [174]. So far, neither of these approaches has been able to provide an unambiguous explanation on the emergence of collective phenomena in small systems. Further experimental inputs are required in order to distinguish them, and finally identify the hadron production mechanisms.

A way to shed more light on the situation is to perform more multi-differential study, typically of the angular and rapidity correlations between different hadron species. These bring informations on the quark production, and consequently on the hadronisation. Two hadrons produced out of the breaking of a colour string into a quark-antiquark pair, as modeled by PYTHIA, should exhibit a strong local correlations. On the other hand, if the quarks are produced in the early stage of the collision – the so-called “prehadrons” in EPOS framework [173] – and hadronise later, that correlation should vanish.

One example of such measurement comes from the PYTHIA experts: since strangeness is conserved by the strong interaction, the number of strange hadrons is expected to be exactly compensated by the number of anti-strange hadrons, leading to a correlation between these hadrons². In particular, within the standard

²As a side note, since all the strange hadrons are correlated, one can control to some extent the strangeness content within an event using a trigger on strange particle, Ξ or Ω for example.

Lund string framework, multi-strange baryons can be produced through a diquark-antidiquark string breaking. However, the “recent” developments towards heavy-ion collisions – namely the colour reconnection and colour rope [175][176][177] – offer new production mechanisms. As a consequence, it is predicted that i) the Ω abundancy increases in presence of a $\phi(1020)$ in the event, and ii) this enhancement gets more prominent as the gap in rapidity between these two particles decreases.

So far, no such correlation has ever been measured. A similar observable has been studied recently [178], that analyses the angular correlations between the multi-strange baryon Ξ^\pm and p^\pm , π^\pm , K^\pm , $\bar{\Lambda}$, Ξ^\pm itself. It was not extended to $\phi(1020)$ resonance nor repeated with Ω baryons, though. Therefore, this analysis aims to check this prediction via the measurement of correlated production of Ω and $\phi(1020)$ over all the pp collisions at a centre-of-mass energy of 13 TeV collected throughout the LHC Run-2 by ALICE. In order to reduce as much as possible the background contamination, such measurement requires a trigger with a high purity, and thus good control capabilities over the amount of signal and the background for the trigger. For that reason and contrarily to the PYTHIA’s prediction, the trigger is on the Ω particles and not the $\phi(1020)$, the former offering a more governable purity.

Since the Ξ baryon is much more produced than the Ω , two measurements are performed : first, the correlated production of Ξ and $\phi(1020)$, and then the one of Ω and $\phi(1020)$. In this way, the feasibility of such measurement can be checked on the Ξ , and if so, it will be repeated with the Ω .

By design, this kind of analysis relies on two categories of particles: the *trigger particles*, which is then correlated to the particles of interest in the event, the *associated particles*. In the present chapter, the term *trigger particle* designates either a Ξ or a Ω baryon, and the *associated particle* corresponds to the $\phi(1020)$ resonance.

II Data samples and event selection

II-A The data samples

Considering their relatively low yield – about 2×10^{-2} Ξ and $\sim 1.85 \times 10^{-3}$ Ω , and $\sim 3.8 \times 10^{-2}$ $\phi(1020)$ at mid-rapidity [142] – the correlation between these particles requires all the data available. Therefore, this second analysis employs the same real and simulated data samples as in the first one, in Chap. 5. It means that all pp collisions at centre-of-mass energy of 13 TeV collected in 2016, 2017 and 2018 are put to use (Sec. 5|II-A).

Contrarily to the first analysis, this one exploits data in AOD format, as it does not necessitate such a fine control over the data reconstruction. The analysed events also come from the second reconstruction cycle, the pass-2.

II-B The event selection

All the event selections employed in the first analysis (Sec. 5|II-B) are also applied here. These are complemented by an additional requirement on the type of

Multiplicity Class	I	II	III	IV	V
$\sigma / \sigma_{\text{INEL}>0}$	0-0.01%	0.01-0.1%	0.1-0.5%	0.5-1%	1-5%
$\langle dN_{\text{ch}}/d\eta \rangle$	$35.37^{+0.92}_{-0.86}$	$30.89^{+0.57}_{-0.51}$	$26.96^{+0.37}_{-0.30}$	$24.23^{+0.36}_{-0.30}$	$20.02^{+0.27}_{-0.22}$
Multiplicity Class	VI	VII	VIII	IX	X
$\sigma / \sigma_{\text{INEL}>0}$	5-10%	10-15%	15-20%	20-30%	30-40%
$\langle dN_{\text{ch}}/d\eta \rangle$	$16.17^{+0.22}_{-0.18}$	$13.77^{+0.19}_{-0.16}$	$12.04^{+0.17}_{-0.14}$	$10.02^{+0.14}_{-0.11}$	$7.95^{+0.11}_{-0.09}$
Multiplicity Class	XI	XII	XIII		
$\sigma / \sigma_{\text{INEL}>0}$	40-50%	50-70%	70-100%		
$\langle dN_{\text{ch}}/d\eta \rangle$	$6.32^{+0.09}_{-0.07}$	$4.50^{+0.07}_{-0.05}$	$2.55^{+0.04}_{-0.03}$		

Table 6.1: Event multiplicity classes, with the corresponding fraction of the total inelastic cross section $\text{INEL} > 0$ ($\sigma / \sigma_{\text{INEL}>0}$) and average charged particle multiplicity at mid-rapidity, $\langle dN_{\text{ch}}/d\eta \rangle$. Table taken from [181][182].

event.

The behaviour of the hadronic interactions at high energies is typically described by the Regge theory[179]. There exists two classes of interaction: the elastic collisions – when the initial and final states of the interaction are the same – and inelastic (INEL) collisions, that involve the production of new particles. The latter subdivides into two categories: the diffractive and non-diffractive processes. The former combines single and double diffractive processes. Within the framework of the Regge theory, the diffractive processes occur respectively when either or both incoming protons become an excited system – due to the exchange of Pomerons –, that later decay into stable final-state particles emitted close to the mother direction, *i.e.* close to beam, at very forward rapidity [180].

This analysis focuses on hadrons produced in inelastic collisions at mid-rapidity, hence originating *a priori* from non-diffractive processes. Experimentally, this kind of inelastic collisions are selected by requiring, at least, one reconstructed SPD tracklet in $|\eta| < 1$. This condition is commonly referred as $\text{INEL} > 0$ ³.

Moreover, two estimators can be considered for the multiplicity determination: the total charge deposited in the VZERO scintillator arrays in $-3.7 < \eta < -1.7$ and $2.8 < \eta < 5.1$ (VZERO-M amplitude, Sec. 5[IV-B.vii]); the number of reconstructed SPD tracklets in $|\eta| < 1$ ($N_{\text{tracklets}}^{|\eta|<1}$). Although the choice between these two estimators seems innocent/arbitrary, notice that they cover different pseudo-rapidity regions: the former estimates the multiplicity (at mid-rapidity) based on the energy deposited at forward rapidity, while the latter counts the number of tracklets at mid-rapidity. This difference may have some implications. Since the observable is a yield ratio at mid-rapidity, the considered particle and/or its decay products may contribute to the number of reconstructed SPD tracklets, thus self-biasing the multiplicity event. In general, the separation between the region of interest and the

³Note that $\text{INEL} > 0$ events do not correspond to the total number of inelastic collisions INEL , due to the acceptance and efficiency of the $\text{INEL} > 0$ condition, the beam-induced background selections, the number of un-reconstructed events (because no preliminary primary vertex could be formed for example, Sec. 3[II-D.i]). In fact, for MB_{AND} , the $\text{INEL} > 0$ encompasses about $76.3^{+2.2}_{-0.8}\%$ of the total number of inelastic collisions [153].

volume covered by the multiplicity estimator should be as large as possible, in order to avoid or limit this auto-correlation. For that reason, the VZERO-M is taken as default multiplicity estimator.

It follows that the events are divided into thirteen multiplicity classes, presented in Tab. 6.1. The Sec. 6|III will show that the reconstruction of cascade and a $\phi(1020)$ resonance in the same event requires at least five tracks. Therefore, the correlations between these two hadrons are measured for events comprised between the 50% with the lowest multiplicity to the 1% with the highest multiplicity,

III Analysis of the multi-strange baryon- $\phi(1020)$ correlation

III-A The correlation function

The objective is to measure the correlation between a multi-strange baryon, either Ξ^\pm or Ω^\pm , and a $\phi(1020)$ meson. Their correlation is evaluated by associating them in pairs, and observing how the pair population is distributed according to a given variable. More precisely, the focus here is on the correlated yield of $\phi(1020)$ meson in events containing, at least, one multi-strange baryon. Therefore, the observable should be the per-trigger yield of the $\phi(1020)$ meson as a function of the difference in p_T , rapidity, azimuthal angle between the trigger particle and the associated particles, and the multiplicity of the event,

$$\frac{1}{N_{\text{trigger}}} \cdot \frac{dN_{\text{pairs}}}{dy} = \frac{1}{dN_{\text{cascade}}/dy} \cdot \frac{dN_{\text{pairs}}}{dy}(\Delta p_T, \Delta\varphi, \Delta y, \text{multiplicity}), \quad (6.1)$$

where the N_{pairs} corresponds to the number of cascade- $\phi(1020)$ pairs.

It will become clear in the next sections that a multi-differential observable such as in Eq. 6.1 cannot be measured currently with the LHC Run-2 data, due to the lack of statistics. Nonetheless, this correlation may still be investigated, although less differentially. Along this line, this analysis proposes to measure the per-trigger yield as a function of one variable at a time, *i.e.*

$$\frac{1}{dN_{\text{cascade}}/dy} \cdot \frac{d^2 N_{\text{pairs}}}{dy d\Delta y}, \quad (6.2)$$

$$\frac{1}{dN_{\text{cascade}}/dy} \cdot \frac{d^2 N_{\text{pairs}}}{dy d\Delta\varphi}, \quad (6.3)$$

$$\frac{1}{dN_{\text{cascade}}/dy} \cdot \frac{d^2 N_{\text{pairs}}}{dy d\Delta p_T}. \quad (6.4)$$

A few words on the analysis strategy before proceeding. ~~Therefore,~~ only events containing a Ξ or Ω candidate are selected; from these, the particles of interest are

reconstructed using the selections in Sec. 6|III-C. After calculating the invariant mass of each candidate, they are sorted as a function of their p_T ⁴ and – only for the particles of interest – the difference of rapidity Δy , azimuthal angle $\Delta\varphi$ and transverse momentum Δp_T with respect to the trigger particle. The yields of both species are extracted from their respective invariant mass distributions, for each p_T , Δp_T , Δy and Δp_T bins, as presented in Sec. 6|III-D.

In the present measurement, the associated particles comprise solely the $\phi(1020)$. However, the analysis has been designed in view of extending the correlations to other kind of hadrons, namely p^\pm , π^\pm , K^\pm , K^{*0} , K_S^0 , $\bar{\Lambda}$, Ξ^\pm and $\bar{\Omega}^\pm$.

Particle	Quark content	Mass (MeV/ c^2)	Lifetime $c\tau$ (cm) or Width Γ (MeV/ c^2)	Dominant decay channel	B.R.
$\phi(1020)$	$s\bar{s}$	1019.461 ± 0.020	$\Gamma = 4.249$	$K^+ K^-$	49.1%
Λ ($\bar{\Lambda}$)	uds ($\bar{u}\bar{d}\bar{s}$)	1115.683 ± 0.006	$c\tau = 7.89$	$p \pi^-$ ($\bar{p} \pi^+$)	63.9%
Ξ^- (Ξ^+)	dss ($\bar{d}\bar{s}\bar{s}$)	1321.71 ± 0.07	$c\tau = 4.91$	$\Lambda \pi^-$ ($\bar{\Lambda} \pi^+$)	99.9%
Ω^- ($\bar{\Omega}^+$)	sss ($\bar{s}\bar{s}\bar{s}$)	1672.45 ± 0.23	$c\tau = 2.461$	ΛK^- ($\bar{\Lambda} K^+$)	67.8%

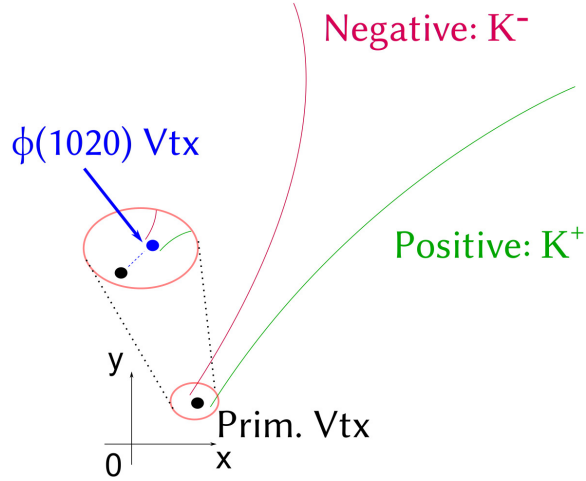
Table 6.2: A few characteristics, as of 2023, of the Λ , Ξ , Ω hyperons and the $\phi(1020)$ meson resonance: quark content, mass, relative mass difference values with their associated uncertainties and their dominant decay channel as well as the corresponding branching ratio [42].

The multi-strange baryons being already introduced in details in Chap. 4 and Chap. 5, we will be concentrating on the $\phi(1020)$ resonance. As presented in Tab. 6.2, it has a mass of 1019.461 MeV and a width of 4.249 MeV, equivalent to a lifetime of approximately 46 fm. It mainly decays via strong interaction into a pair of oppositely charged kaons with a branching ratio of 49.1%, $\phi(1020) \rightarrow K^+ K^-$, as depicted in Fig. 6.3. In the following, the $\phi(1020)$ will be studied in this decay channel.

The $\phi(1020)$ resonance is reconstructed by forming pairs of oppositely charged tracks; similarly to the V0s, the positively charged daughter is called the *positive* particle, the other the *negative* particle. As a consequence of the strong nature of the decay, its short flight distance makes the decay vertex undistinguishable from the primary interaction point. Thereby, the misassociated pairs cannot be discarded using geometrical selections – as opposed to the topological reconstruction of V0s and cascades –, leading to a substantial combinatorial background. This is the reason why it was decided to consider the multi-strange baryons as trigger particles, instead of the $\phi(1020)$ resonance meson. This background can be evaluated and subtracted by making use of two techniques here, presented later in Sec. 6|III-C.

⁴This is necessary in order to correct for the detector acceptance and the reconstruction efficiency (Sec. 6|III-F).

Fig. 6.3: Scheme of the resonance decay of the $\phi(1020)$ meson. Modified version of the original figure [139].




III-B Cascade candidate selections

As in Chap. 5, the identification of multi-strange baryons relies on their characteristic cascade decay channel. Their reconstruction therefore exploits the same topological and kinematic selection variables, Sec. 5|III-A and 5|III-B. These are presented in Tab. 6.3.


There is however one important difference with respect to the first analysis. While the latter measures the mass integrated over all the p_T bins⁵, the objective here is to extract the yield of both trigger and associated particles, these being obtained from their p_T -differential production rate.

$$\frac{dN}{dy} = \int_0^{+\infty} \frac{d^2N}{dp_T dy} dp_T \quad (6.5)$$

Thereby, the candidates are sorted as a function of their transverse momentum according to, for Ξ^\pm baryons, thirteen p_T intervals:

[0.6;1.0) GeV/c, [1.0;1.2) GeV/c, [1.2;1.4) GeV/c, [1.4;1.6) GeV/c, [1.6;1.8) GeV/c, [1.8;2.0) GeV/c, [2.0;2.2) GeV/c, [2.2;2.5) GeV/c, [2.5;2.9) GeV/c, [2.9;3.4) GeV/c, [3.4;4.0) GeV/c, [4.0;5.0) GeV/c, [5.0;6.5) GeV/c. 

For what concerns the measurement of the $\bar{\Omega}^\pm$ hyperons, due to their lower statistics, six intervals are being used:

[1.0;1.6) GeV/c, [1.6;2.2) GeV/c, [2.2;2.6) GeV/c, [2.6;3.0) GeV/c, [3.0;3.8) GeV/c, [3.8;6.5) GeV/c. 

III-C Resonance candidate selections

As explained in the header of this section, the $\phi(1020)$ meson candidates are reconstructed as a pair of K^+ and K^- . Since the decay topology cannot be exploited

⁵There is one exception in Sec. 5|IV-B.iii, where the p_T -differential measurement of the mass is performed in order to check the stability of the results with the transverse momentum.



Candidate variable	Selections Ξ^{\pm}	Selections $\bar{\Omega}^{\pm}$
Cascade p_{T} interval (GeV/c)	$0.6 < p_{\text{T}} < 6.5$	
Cascade rapidity interval	$ y < 0.5$	
Competing mass rejection (GeV/c ²)		> 0.008
MC association (MC only)	Correct identity assumption	
Track variable	Selections Ξ^{\pm}	Selections $\bar{\Omega}^{\pm}$
Pseudo-rapidity interval	$ \eta < 0.8$	
TPC refit		
Nbr of crossed TPC readout rows	> 70	
n_{σ}^{TPC}	< 3	
Out-of-bunch pile-up rejection	at least one track with ITS-TOF matching	
Topological variable	Selections Ξ^{\pm}	Selections $\bar{\Omega}^{\pm}$
V0		
V0 decay radius (cm)	> 1.2	> 1.1
V0 cosine of pointing angle	> 0.97	
$ m(V0) - m_{\text{PDG}}\Lambda $ (GeV/c ²)	< 0.008	
DCA proton to prim. vtx (cm)	> 0.03	
DCA pion to prim. vtx (cm)	> 0.04	
DCA V0 to prim. vtx (cm)	> 0.06	
DCA between V0 daughters (std dev)	< 1.5	
Cascade		
Cascade decay radius (cm)	> 0.6	> 0.5
Cascade Lifetime (cm)	$< 3 \times c\tau$	
DCA bachelor to prim. vtx (cm)	> 0.04	
DCA between cascade daughters (std dev)	< 1.3	
Cascade cosine of pointing angle	> 0.998	
Bachelor-proton pointing angle (rad)	> 0.04	

Table 6.3: Summary of the topological and track selections, as well as the associated cut values, used in the reconstruction of Ξ^{\pm} and $\bar{\Xi}^{\pm}$ in pp events at $\sqrt{s} = 13$ TeV. The *competing mass rejection* refers to the removal of the background contamination from other mass hypotheses (Sec. 4|II-B.iii)

to reduce the amount of combinatorial background, most of the selection criteria focus on the quality of daughter tracks⁶. These can be found in Tab. 6.4.

Beyond the track selections in common with the hyperons (Sec. 5|III-A), the track quality is improved by requiring a reduced χ^2 up to 36 and 4, for the ITS and TPC standalone tracks respectively⁷. The agreement between the TPC standalone

⁶In this analysis, the focus is on the $\phi(1020)$ yield in presence of a multi-strange baryon. However, note that the same considerations would also apply in the case of the K^{*0} resonance, that decays strongly into a K^{\pm} and a π^{\pm} at $\sim 100\%$.

⁷The tighter selection on the goodness of the TPC standalone track is related to the fact that TPC is the main tracking device in ALICE and so, contributes the most to the track quality.

Candidate variable	Selection criterion
Resonance rapidity interval	$ y < 0.5$
MC association (MC only)	Correct identity assumption
Track variable	Selection criterion
p_T interval (GeV/c)	$0.15 < p_T < 20$
Pseudo-rapidity interval	$ \eta < 0.8$
ITS refit	✓
TPC refit	✓
Kink Topology	✗
n_{σ}^{TPC}	< 2
n_{σ}^{TOF} (veto only)	< 3
Nbr of crossed TPC readout rows	> 70
Fraction of crossed TPC readout rows over findable clusters	≥ 0.8
Goodness of the TPC standalone track, $\chi_{\text{TPC}}^2/N_{\text{cluster}}$	< 4
Global and TPC standalone track matching, $\chi_{\text{TPC-CG}}^2$	< 36
Goodness of the ITS standalone track, $\chi_{\text{ITS}}^2/N_{\text{cluster}}$	< 36
Nbr of associated SPD clusters	≥ 1
DCA to prim. vtx (cm)	$< 0.0105 + 0.035 p_T^{-1.01}$
DCA to prim. vtx along z (cm)	< 2

Table 6.4: Summary of the track and candidate selections used for the reconstruction of $\phi(1020)$.

track, constrained to the preliminary primary vertex (Sec. 3|II-D), and global track is quantified by the so-called *golden* χ^2 ; its value should be smaller than 36. Along the same line, each track must have passed the final refit in the ITS, and be associated with at least one hit in the innermost ITS layers, the most granular detector in ALICE. To ensure a good momentum resolution, the fraction of found crossed TPC readout rows over the number of findable clusters must reach at least 80%.

Since the decay point cannot be resolved from the primary vertex, the formation of a resonance candidate uses primary tracks, contrarily to the V0 and cascade reconstruction. These are identified by imposing that their distance of closest approach to the primary vertex is smaller than a critical value. In particular, in the transverse plane, the latter is given by a p_T -dependent *ad-hoc* formula in order to be even more selective.

Further combinatorial background is suppressed by applying PID criteria. It is required that each track agrees with a K^\pm mass hypothesis within $n_{\sigma}^{\text{TPC}} = \pm 3$. Whenever it matches a hit in the TOF detector⁸, the time-of-flight informations supplement the selection on the nature of the decay daughter using the PID estimator in Eq. 3.6, n_{σ}^{TOF} .

⁸Since a substantial amount of particles do not reach the TOF detector or cannot be matched with a hit, the associated hadron identification capabilities can only be used as a veto, in complement to other PID informations; otherwise, this would drastically affect the track reconstruction efficiency.

Finally, any pair of tracks satisfying the above criteria and lying at mid-rapidity, $|y| < 0.5$, is considered as a $\phi(1020)$ meson candidate. Their measurement is performed in the following eight p_T intervals:

$[0.4; 0.8)$ GeV/ c , $[0.8; 1.2)$ GeV/ c , $[1.2; 1.8)$ GeV/ c , $[1.8; 2.6)$ GeV/ c , $[2.6; 3.4)$ GeV/ c , $[3.4; 4.2)$ GeV/ c , $[4.2; 5)$ GeV/ c , $[5; 11)$ GeV/ c .

III-D The raw signal extraction

III-D.i In the case of multi-strange baryons

The raw signal extraction for the trigger particle follows the very same procedure as in the first analysis. Therefore, the invariant mass peak is modeled by a modified Gaussian (Eq. 5|III-C.ii), and the background by a linear function. The amount of raw signal and background are estimated by bin counting, over the same regions as in Sec. 5|III-C.

The Figs. 6.4, 6.5 show the invariant mass distribution in the different p_T intervals for Ξ^- , Ξ^+ , Ω^- and $\bar{\Omega}^+$ respectively.

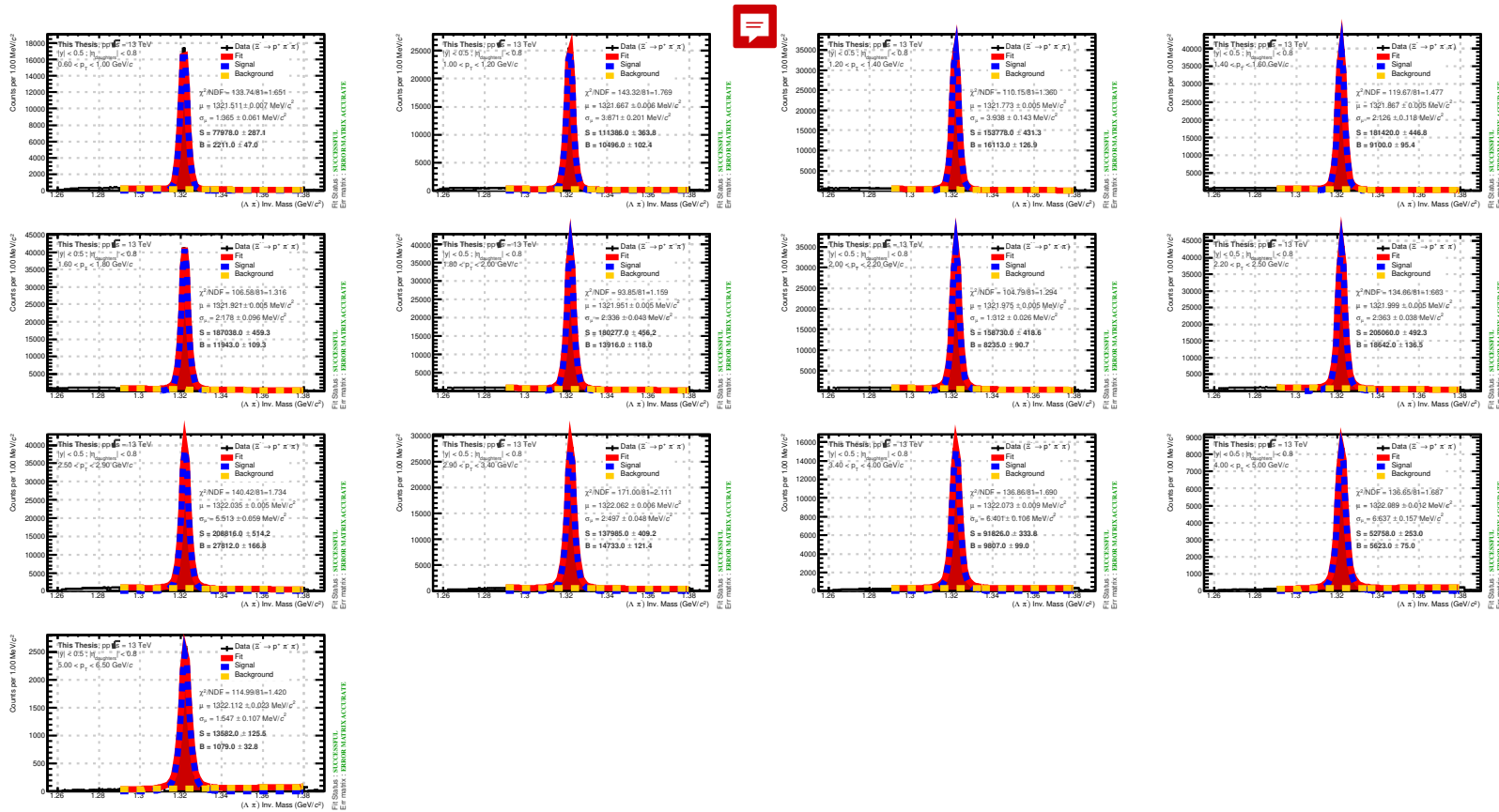


Fig. 6.4: Invariant mass spectra of the Ξ^- candidates in pp collisions at $\sqrt{s} = 13$ TeV, fitted by the combination of three Gaussian functions for the peak and a decreasing exponential function for the background. The amounts of signal and background have been obtained via bin counting in the peak (red area) and side-bands region (gray area).

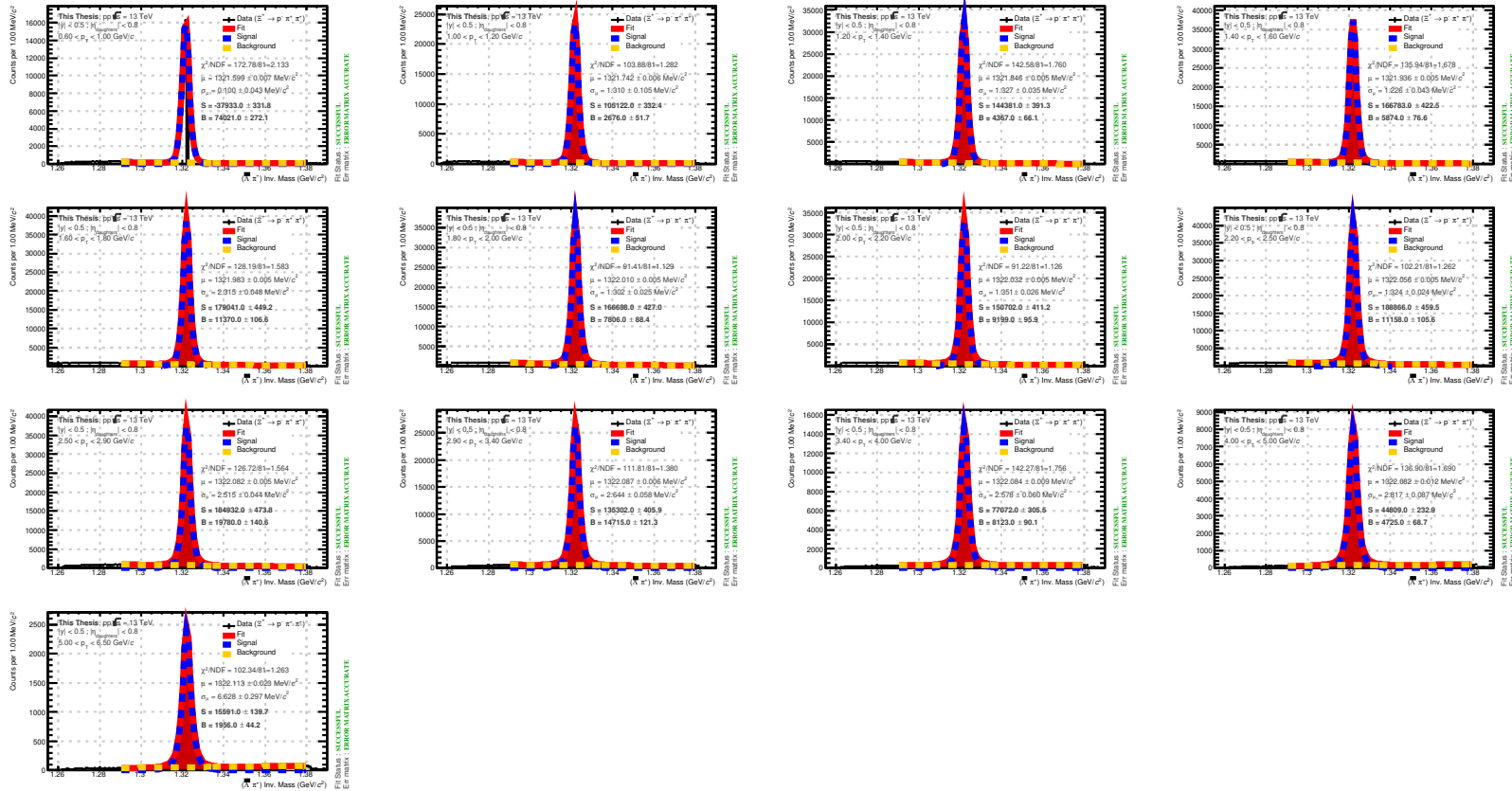


Fig. 6.5: Invariant mass spectra of the Ξ^- candidates in pp collisions at $\sqrt{s} = 13$ TeV, fitted by the combination of three Gaussian functions for the peak and a decreasing exponential function for the background. The amounts of signal and background have been obtained via bin counting in the peak (red area) and side-bands region (gray area).

III-D.ii In the case of $\phi(1020)$ meson

The invariant mass of each resonance candidate is calculated using the Eq. 6.8 and making the assumption of a K^\pm mass for both decay daughters. The top left Fig. 6.6 present the invariant mass spectra of the $\phi(1020)$ meson for every p_T intervals.

$$M_{\text{candidate}}^2[\phi(1020)] = (E_{\text{pos.}} + E_{\text{neg.}})^2 - (\vec{p}_{\text{pos.}} + \vec{p}_{\text{neg.}})^2 \quad (6.6)$$

$$= \left(\sqrt{\vec{p}_{\text{pos.}}^2 + m_{\text{pos.}}^2} + \sqrt{\vec{p}_{\text{neg.}}^2 + m_{\text{neg.}}^2} \right)^2 - (\vec{p}_{\text{pos.}} + \vec{p}_{\text{neg.}})^2 \quad (6.7)$$

$$= \left(\sqrt{\vec{p}_{\text{pos.}}^2 + m_{K^+}^2} + \sqrt{\vec{p}_{\text{neg.}}^2 + m_{K^-}^2} \right)^2 - (\vec{p}_{\text{pos.}} + \vec{p}_{\text{neg.}})^2 \quad (6.8)$$

An excess of counts emerges around the tabulated mass of the $\phi(1020)$, $m_{\text{PDG}} = 1019.461 \text{ MeV}/c^2$, on top of a smooth background. The latter dominates the invariant mass distribution, and derives *a priori* mainly from combinatorics of the tracks. The origin of the background being known, it can thus be removed⁹. The basic idea consists to reproduce the background shape by forming uncorrelated pairs of tracks. There exist two approaches¹⁰:

- **Event mixing technique:** by definition, particles originating from different events could not have been produced together, and so are uncorrelated. Consequently, the association of tracks from different events should *in principle* result in combinatorial background. This is core concept of event mixing. Therefore, each positively charged track passing the above selections (Sec. 6|III-C) gets paired to a negatively charged track from another event, under the exact same set of cuts, and vice versa. Each event is mixed with five other events at most. In order to estimate correctly the combinatorial background, the mixing has to be performed between events with similar collision kinematics. To ensure that, it is required that i) the longitudinal position of their primary vertex agrees within a range of $\pm 1 \text{ cm}$, and ii) their difference in terms of event multiplicity should be sufficiently low, such that they belongs to the same multiplicity class. Moreover, since the several events are involved in the mixing, the mixed-event invariant mass distribution needs to be normalised, such that it fits the same-event distribution in certain invariant mass region. This normalisation is usually performed far from the peak, in the side-bands regions purely populated by combinatorial background.
- **Rotating procedure:** the excess of counts in the invariant mass distributions originates from correlated pairs of K^+ and K^- due to the $\phi(1020)$ meson decay. If the correlation of the pair could somehow be broken, the invariant mass

⁹Alternatively, one could try to find a functional form that describes correctly the shape of the background, as it was done in Chap. 5. For instance, here, it could be modeled by a second order polynomial.

¹⁰In fact, there also exist a third approach. These resonances are formed out of two oppositely charged, *i.e.* unlike-charge, tracks. Particles of the same charge are uncorrelated with respect to the $\phi(1020)$ decay. Hence, by pairing like-charge tracks, $K^+ K^+$ and $K^- K^-$, the combinatorial background can be estimated. However, this procedure has been implemented in the analysis, and so will not be used.

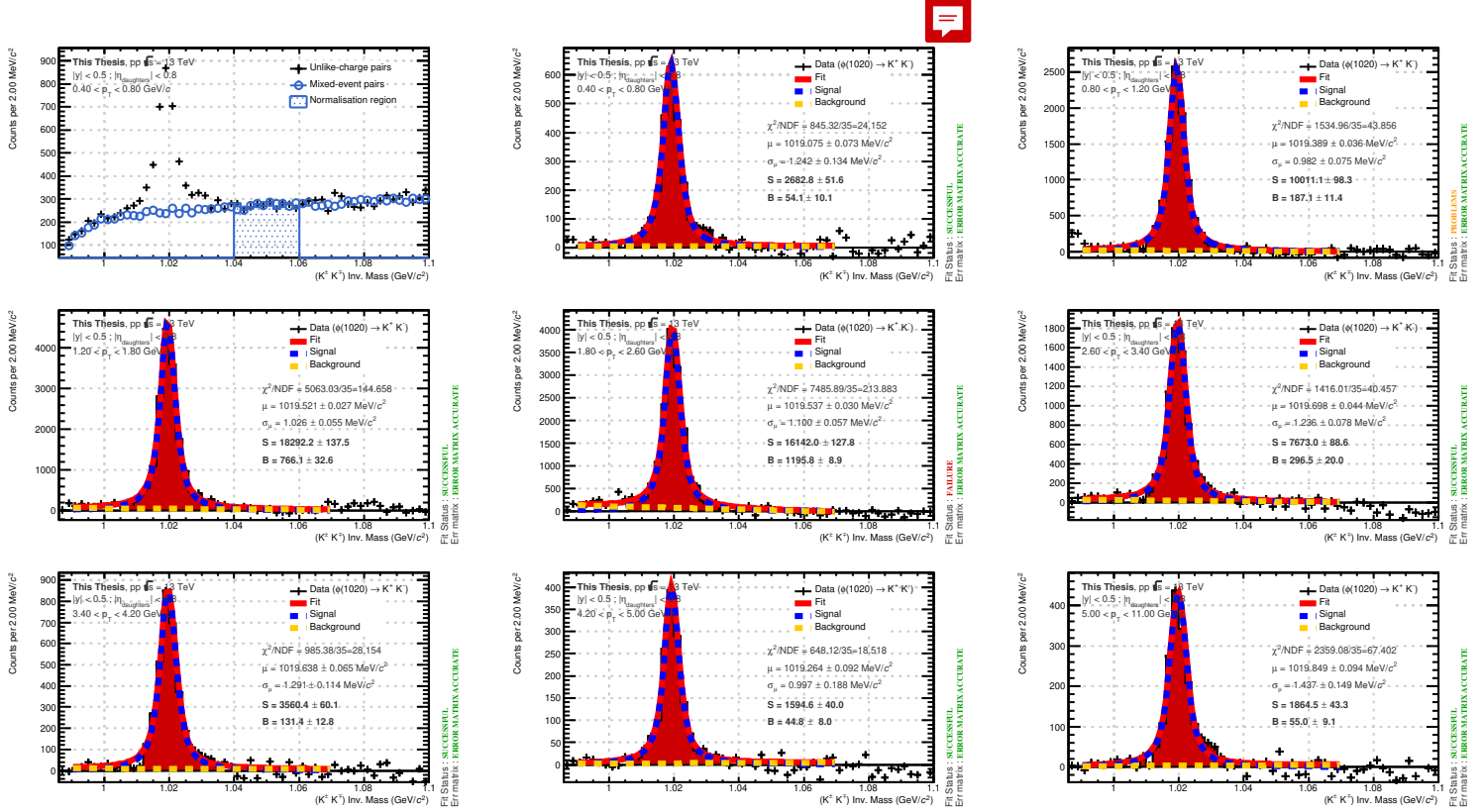


Fig. 6.6: Top left panel: Unlike-charge and mixed-event invariant mass distribution for p_T between 0.4 and 0.8 GeV/c. The other panels: Invariant mass spectra of the $\phi(1020)$ meson candidates in pp collisions at $\sqrt{s} = 13$ TeV, fitted by the sum of a Voigt function for the peak and a linear function for the residual background. The amounts of signal have been obtained as explained in Sec. 6|III-D.ii, while the background has been obtained via bin counting in the region covered by the red area, that is 1.005 and 1.035 GeV/c².

spectrum should be populated solely by combinatorial background. This can be achieved by considering the already formed pairs of kaons from the same event and rotating one of track by a significant amount, typically by an angle of 180°.

The event mixing technique is taken as the default option, as it will later facilitate another part of the analysis Sec. 6|V-B. The rotating procedure is going to be used in the systematic study.

Whatever the considered approach, the combinatorial background is subtracted from the invariant distribution, yielding to the Figs. 6.6. The invariant mass now sits on top of a small residual background. The signal is separated from the background through a (log-)likelihood method.

The ideal signal for a resonance should exhibit a Breit-Wigner shape [183]. However, the invariant mass peak rather corresponds to the convolution of Breit-Wigner and Gaussian – due to the smearing induced by the detectors response – distributions, namely the Voigt profile in Eq. 6|III-D.ii.

$$\frac{dN}{dm_{\text{inv}}} = A \cdot \frac{\Gamma}{(2\pi)^{3/2}\sigma} \int_{-\infty}^{\infty} \exp\left[-\frac{(m_{\text{inv}} - m')^2}{2\sigma^2}\right] \frac{1}{(m' - \mu)^2 + \Gamma^2/4} dm', \quad (6.9)$$

where:

- A coincides with the integral of the function from 0 to $+\infty$,
- μ corresponds to the centre of the Voigt function,
- Γ is the resonance width,
- and σ describes the width of the Gaussian.

Only this function is considered for the peak description. Here, two types of Voigtian fits are considered: one with the resonance width fixed at the nominal value ($\Gamma = 4.249 \text{ MeV}/c^2$), the other where it is allowed to vary freely. Concerning the residual background, as in the first analysis, different shapes can be considered: constant, linear, exponential functions, second order polynomial.

If the fitting procedure converges, the signal and background are estimated. As the Voigt function (resonance case) does not decrease as fast as a Gaussian (multi-strange baryon case) with the distance to centre, the amount of raw signal and background have to be evaluated differently. In this context, the peak region is defined in $[1.005; 1.035] \text{ GeV}/c^2$, and contains most of the signal and some background. Therefore, the raw signal is obtained by counting the number of candidates in this region and subtracting the background population; the latter is given by the integral of the background function over the same region, hence $S_{\text{counting}} = (S + B)_{\text{counting}} - B_{\text{integral}}$. The rest of the signal population sits outside the peak region, from 0.987354^{11} to $1.005 \text{ GeV}/c^2$ and 1.035 to $+\infty \text{ GeV}/c^2$. Consequently, the integral of the Voigt function in these two regions provides an estimation of the missing signal population, which is then incorporated in the total raw signal $S = S_{\text{counting}}(1.005; 1.035) + S_{\text{integral}}(0.987354; 1.005) + S_{\text{integral}}(1.035; +\infty)^{12}$.

III-E Fraction of background cascade

As explained [in the header](#) of this section, the correlation between cascade and resonances goes through pairs of particle candidates. Thereby, as illustrated in Tab. 6.5, there exist four types of pairs depending on whether they are signal or background candidates.

In the ideal case, only correlation between a true Ξ^{\pm} or $\bar{\Xi}^{\pm}$ and an actual $\phi(1020)$ should be observed. As explained in Sec. 6|III-C, the contribution from the background resonances is already removed bin-by-bin first using an event mixing technique, and then the raw signal of $\phi(1020)$ is isolated from the residual background through a fit with a linear function. The only remaining source of correlation with background candidate comes from the multi-strange baryons. Considering the

¹¹It corresponds to $2m_{K^{\pm}} = 0.987354 \text{ GeV}/c^2$ with $m_{K^{\pm}} = 0.493677 \text{ GeV}/c^2$ [42]. The population of $\phi(1020)$ cannot be found below this mass value because it is kinematically forbidden.

¹²In the analysis, the peak function is not integrated to + infinity, but rather up to a large mass value with respect to the $\phi(1020)$ mass – that is $5 \text{ GeV}/c^2$ – such that most of the missing raw signal has been taken into account.

Ξ^\pm or $\bar{\Xi}^\pm$ $\phi(1020)$	Signal candidate	Background candidate
Signal candidate	Signal-Signal	Signal-Background
Background candidate	Background-Signal	Background-Background

Table 6.5: Four types of cascade-resonance correlation in the analysis, depending on the cascade and resonance candidates. The red cells represent the correlations with a background trigger candidate, that must be removed.

purity of the sample, the contribution of the cascade background candidates could be assumed as negligible. This means that

$$\frac{1}{N_{\text{trigger}}} \cdot \frac{d^2 N_{\text{pairs}}}{dydX} = \frac{1}{N_{\text{trigger}}(S)} \cdot \frac{d^2 N_{\phi(1020)}}{dydX} \Big|_{(S) \text{ trigger} - (S) \text{ associated pairs}} \quad (6.10)$$

$$\simeq \frac{1}{N_{\text{trigger}}(S+B)} \cdot \frac{d^2 N_{\text{pairs}}}{dydX} \Big|_{(S+B) \text{ trigger} - (S) \text{ associated pairs}}, \quad (6.11)$$

where X corresponds to either Δy , $\Delta \varphi$ or Δp_T , $(S+B)$ signifies signal and background candidates, and (S) is for pure signal candidates.

An attempt is made to get as precise as possible. To that end, two measurements are performed: one in which cascades in the peak region are correlated to resonance candidates, and another with cascades from the side-bands region instead. Each of them provides a set of invariant mass distributions for the associated particles as a function of their rapidity, azimuthal angle and/or transverse momentum gap with respect to the trigger particle.

$$\frac{1}{N_{\text{trigger}}} \cdot \frac{d^2 N_{\phi(1020)}}{dydX} = \frac{1}{N_{\text{trigger}}(S)} \cdot \frac{d^2 N_{\phi(1020)}}{dydX} \Big|_{(S) \text{ trigger} - (S) \text{ associated pairs}} \quad (6.12)$$

$$= \frac{1}{N_{\text{trigger}}(S+B) - N_{\text{trigger}}(B)} \cdot \left[\frac{d^2 N_{\phi(1020)}}{dydy} \Big|_{(S+B) \text{ trigger}} - \frac{dN_{\phi(1020)}}{dy} \Big|_{(B) \text{ trigger}} \right]. \quad (6.13)$$

III-F Acceptance and efficiency corrections

The raw signal quantifies the amount of multi-strange baryons or $\phi(1020)$ resonances reconstructed within the acceptance of the ALICE detector, and satisfying the selections in Tabs. 5.3 and 6.4. In fact, this quantity corresponds to a fraction of the total number of particles produced in the fiducial volume $|y| < 0.5$ due to i) the limited acceptance of the detector that prevents the reconstruction of tracks within certain region of the ALICE apparatus (beyond $|\eta| < 0.8$, deadzones), and ii) the finite reconstruction and selection efficiencies of the cascade and resonance decays. This fraction can be estimated using MC simulations.

In principle, the correction on the raw signal breaks down into two terms, one for each of the aforementioned contributions: the *acceptance*, that corresponds

to the fraction of reconstructable particles in the fiducial volume among the total number of generated particles within the desired rapidity region ($|y| < 0.5$), and the *efficiency* given by the ratio of the number of reconstructed hadrons over the number of reconstructable ones in the same rapidity interval. The product of these two terms provides the acceptance and efficiency correction factors (Eq. 6.14).

$$\text{Acceptance} \times \text{Efficiency} = \frac{N_{\text{daughter in acc.}}^{\text{generated in } |y| < y_{\text{fid.}}}}{N_{\text{generated in } |y| < 0.5}} \times \frac{N_{\text{reconstructed in } |y| < y_{\text{fid.}}}}{N_{\text{daughter in acc.}}^{\text{generated in } |y| < y_{\text{fid.}}}} \quad (6.14)$$

$$= \frac{N_{\text{reconstructed in } |y| < y_{\text{fid.}}}}{N_{\text{generated in } |y| < 0.5}} \quad (6.15)$$

For the sake of simplicity, instead of evaluating these correction factors individually, this analysis goes directly for the product of the two (Eq. 6.15). Since the above selections ~~impact~~ differently low- p_T and high- p_T candidates, these acceptance and efficiency correction factors do depend strongly on the transverse momentum. Therefore, they have to be determined for every p_T -bin. Moreover, note that the branching ratio of the considered particle stands as an upper bound for the reconstruction efficiency, and so for the acceptance \times efficiency.

These corrections aim to compensate for the un-detected and/or un-reconstructed particles in the analysis. Hence, most of the measurements apply such corrections on both trigger and associated particles. While this makes sense in the latter case, it is more dubious for the former ones: by correcting the cascade raw signal, one increases basically the number of such hadrons in the analysis. Those being used as a trigger, it also amounts to increase the number of triggered events. Depending on whether those additional/corrected events contains a $\phi(1020)$ meson or not, whether they are reconstructed or not, whether they are correlated to the trigger particle or not, this will most certainly affect the estimation of the $\Xi^{\pm}-\phi(1020)$ and $\bar{\Omega}^{\pm}-\phi(1020)$ correlations. If, as depicted in the left panel of Fig. 6.7, such correlation in non-triggered event turns out to be small, the previous concerns may reasonably be neglected in first approximation. Conversely, in the configuration shown in the right panel of Fig. 6.7, one should be extremely cautious on how to correct the trigger particle yield.

Due to the non-trivial application of the acceptance \times efficiency correction factors on the trigger particle, the present measurement restricts only to correlations in triggered events. This means that the acceptance and efficiency corrections concern solely the associated particles, namely the $\phi(1020)$.

IV Study of the systematic uncertainties

IV-A Topological and track selections

Selections inspired from the first analysis and [157].

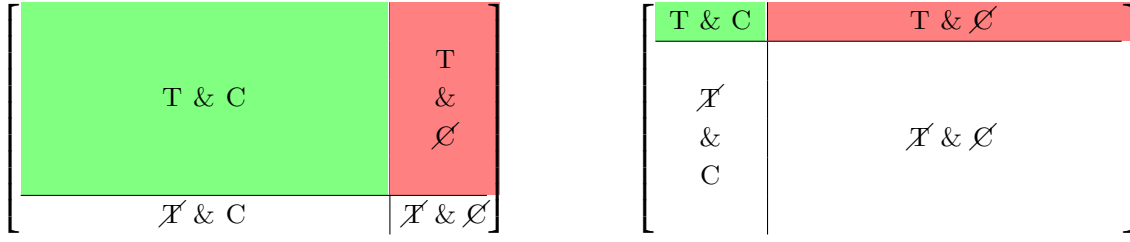


Fig. 6.7: Study of the correlated yield between the trigger and associated particles in two different cases. The area occupied by each cell provides its relative contribution to the correlated production. Four contributions are considered: a trigger particle has been found/detected/reconstructed in the event (T) and it is correlated to at least one associated particle (C); there is no correlation between these particles (T & \emptyset); a trigger particle is present and correlated to an associated particle, though it is not reconstructed (\cancel{T} & C); the trigger particle is not found and is not correlated to the particle of interest (\cancel{T} & \emptyset). The green area corresponds to the measurement at stake, while the red zone represents the contribution accounted for in Sec. 6|V-B. The un-coloured areas are not seen in the present analysis.

IV-A.i Multi-strange baryon identification

IV-A.ii $\phi(1020)$ meson identification

[184]

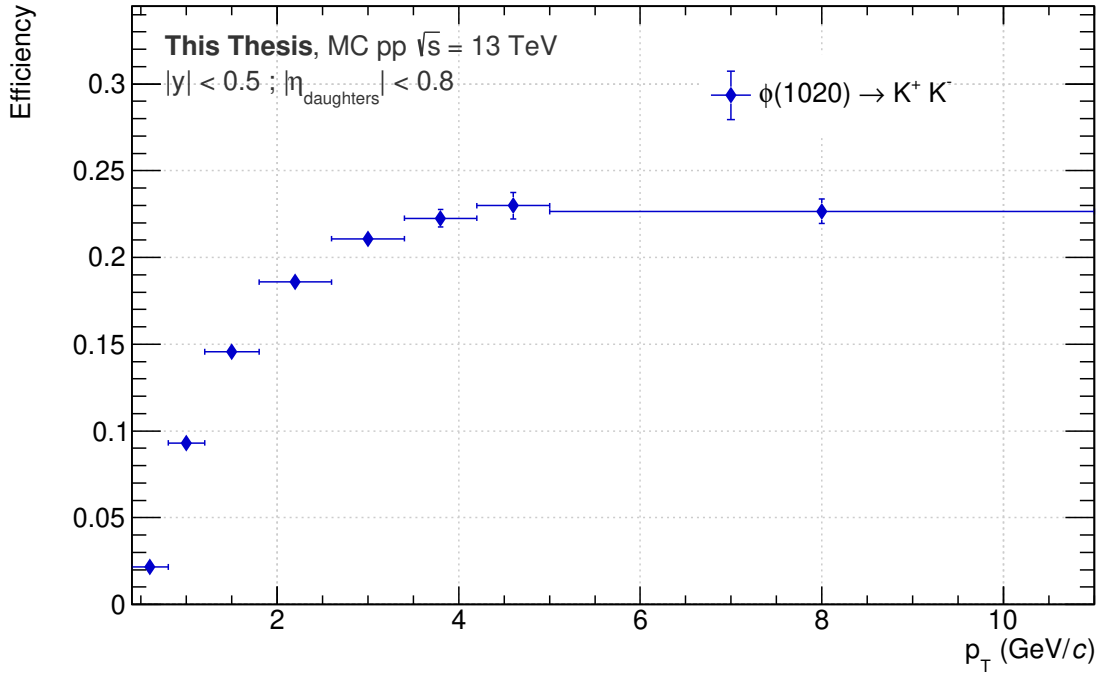


Fig. 6.8: Top left panel: Unlike-charge and mixed-event invariant mass distribution for p_T between 0.4 and 0.8 GeV/c. The other panels: Invariant mass spectra of the $\phi(1020)$ meson candidates in pp collisions at $\sqrt{s} = 13$ TeV, fitted by the sum of a Voigt function for the peak and a linear function for the residual background. The amounts of signal have been obtained as explained in Sec. 6|III-D.ii, while the background has been obtained via bin counting in the region covered by the red area, that is 1.005 and 1.035 GeV/c².

Track variable	Very loose	Loose	Default	Tight	Very tight
Nbr of crossed TPC readout rows			> 70	> 80	> 90
n_{σ}^{TPC}	< 5	< 4	< 3	< 2.5	< 2
Topological variable					
V0					
V0 decay radius (cm)	> 1	> 1.1	> 1.2	> 3	> 5
V0 cosine of pointing angle			> 0.97	> 0.98	> 0.99
$ m(V0) - m_{\text{PDG}}\Lambda $ (GeV/ c^2)	< 0.010	< 0.009	< 0.008	< 0.007	< 0.006
DCA proton to prim. vtx (cm)			> 0.03	> 0.07	> 0.1
DCA pion to prim. vtx (cm)		> 0.03	> 0.04	> 0.15	> 0.3
DCA V0 to prim. vtx (cm)			> 0.06	> 0.1	> 0.13
DCA between V0 daughters (std dev)	< 2	< 1.8	< 1.5	< 1.2	< 1.0
Cascade					
Cascade decay radius (cm)	> 0.4	> 0.5	> 0.6	> 0.8	> 1
Cascade Lifetime (cm)	< 5 $c.\tau$	< 4 $c.\tau$	< 3 $c.\tau$	< 2.5 $c.\tau$	
DCA bachelor to prim. vtx (cm)		> 0.03	> 0.04	> 0.1	> 0.17
DCA between cascade daughters (std dev)	< 2	< 1.6	< 1.3	< 1.0	< 0.8
Cascade cosine of pointing angle	> 0.99	> 0.995	> 0.998	> 0.9985	> 0.999
Bachelor-proton pointing angle (rad)	> 0.02	> 0.03	> 0.04	> 0.045	> 0.05

Table 6.6: Summary of the five configurations – the default as well as four variants – on the topological and track selections employed in the identification the Ξ^{\pm} in pp events at $\sqrt{s} = 13$ TeV. When a value is missing, the preceding selection is considered. These sets of selections have been determined based on the signal variation study carried out in the first analysis (Sec. 5[IV-A]), in conjunction with the ones used in [157].

Candidate variable	Very loose	Loose	Default	Tight	Very tight
Competing mass rejection (GeV/c ²)	> 0.006	> 0.007	> 0.008	> 0.009	> 0.010
Track variable					
Nbr of crossed TPC readout rows			> 70	> 80	> 90
n_{σ}^{TPC}	< 5	< 4	< 3	< 2.5	< 2
Topological variable					
V0					
V0 decay radius (cm)		> 1.0	> 1.1	> 2.5	> 3.5
V0 cosine of pointing angle			> 0.97	> 0.98	> 0.99
$m(V0) - m_{\text{PDG}}\Lambda$ (GeV/c ²)	< 0.010	< 0.009	< 0.008	< 0.007	< 0.006
DCA proton to prim. vtx (cm)			> 0.03	> 0.07	> 0.1
DCA pion to prim. vtx (cm)		> 0.03	> 0.04	> 0.15	> 0.3
DCA V0 to prim. vtx (cm)			> 0.06	> 0.08	> 0.1
DCA between V0 daughters (std dev)	< 2	< 1.8	< 1.5	< 1.2	< 1.0
Cascade					
Cascade decay radius (cm)	> 0.3	> 0.4	> 0.5	> 0.6	> 0.8
Cascade Lifetime (cm)	< 5 $c\tau$	< 4 $c\tau$	< 3 $c\tau$	< 2.5 $c\tau$	
DCA bachelor to prim. vtx (cm)		> 0.03	> 0.04	> 0.08	> 0.1
DCA between cascade daughters (std dev)	< 2	< 1.6	< 1.3	< 1.0	< 0.6
Cascade cosine of pointing angle	> 0.99	> 0.995	> 0.998	> 0.9985	> 0.999
Bachelor-proton pointing angle (rad)	> 0.02	> 0.03	> 0.04	> 0.045	> 0.05

Table 6.7: Summary of the five configurations – the default as well as four variants – on the topological and track selections employed in the identification the $\bar{\Omega}^{\pm}$ in pp events at $\sqrt{s} = 13$ TeV. When a value is missing, the preceding selection is considered. These sets of selections have been determined based on the signal variation study carried out in the first analysis (Sec. 5[IV-A]), in conjunction with those used in [157].

Track variable	Default	Variations			
n_{σ}^{TPC}	< 3	< 2.5	< 3.5	< 3	< 3
n_{σ}^{TOF} (veto only)	< 3	< 3	< 3	veto off	< 4
Nbr of crossed TPC readout rows	> 70	> 80	> 90		
Fraction of crossed TPC readout rows over findable clusters	≥ 0.8	≥ 0.9			
Goodness of the TPC standalone track, $\chi_{\text{ITS}}^2/N_{\text{cluster}}$	< 36	< 25	< 4		
Goodness of the TPC standalone track, $\chi_{\text{TPC}}^2/N_{\text{cluster}}$	< 4	< 2.3			
Global and TPC standalone track matching, $\chi_{\text{TPC-CG}}^2$	< 36	< 25			
Nbr of associated SPD clusters	≥ 1	≥ 0			
DCA to prim. vtx (cm)	$< 0.0105 + 0.035 p_{\text{T}}^{-1.01}$	$< 0.006 + 0.020 p_{\text{T}}^{-1.01}$			
DCA to prim. vtx along z (cm)	< 2	< 1	< 0.2		

Table 6.8: Summary of the variations for each track candidate selections used for the reconstruction of $\phi(1020)$ resonances. Contrarily to the hyperon case, each variation for a given variable is tested individually, while keeping the other variables fixed at their nominal values. The only exception concerns the PID variables, where a pair of TPC and TOF selections gives one configuration. This set of variation has been taken from [184].

IV-B Other sources of systematic uncertainties

- the choice of the fit function
- the imprecision on the material budget

V Results

V-A Summary of the systematic uncertainties

V-B Accounting for the uncorrelated cascade-resonance pairs

As for the $\phi(1020)$ meson reconstruction, there is no way to tell *a priori* which cascade is correlated to a resonance. All the possible combinations have to be exhausted. This inevitably leads to the formation of uncorrelated cascade- $\phi(1020)$ pairs.

Such contribution can be removed using the exact same methods as those used for subtracting the combinatorial background of the resonances: either via an event mixing technique or rotating procedure (Sec. 6|III-C). Our choice went on the first option, purely for simplicity. On the practical side, by re-using the same mixed-event list as for the $\phi(1020)$, the longest part of procedure is already done, making the implementation of the event mixing technique straightforward.

The whole analysis chain needs to be repeated, including the previous elements Sec. 6|III-E and 6|III-F.

V-C Discussion and conclusion